

Presented at the AMPM 2016 conference on Additive Manufacturing, held with MPIF / APMI International Conference on Powder Metallurgy & Particulate Materials in Boston, USA, in June 2016.

## Binder-jetting additive manufacturing with water atomized iron powders

Karine Inaekyan<sup>1</sup>, Vladimir Paserin<sup>2</sup>, Ian Bailon-Poujol<sup>2</sup>, and Vladimir Brailovski<sup>1\*</sup>

1.École de technologie supérieure, 1100 Notre-Dame Street West, Montréal (Québec) H3C 1K3, Canada

2. QMP, Rio Tinto Metal Powders, 1655, route Marie-Victorin, Sorel-Tracy (Quebec) J3R 4R4, Canada

[karine.inaekyan@etsmtl.ca](mailto:karine.inaekyan@etsmtl.ca), [vladimir.paserin@riotinto.com](mailto:vladimir.paserin@riotinto.com), [ian.bailon-poujol@riotinto.com](mailto:ian.bailon-poujol@riotinto.com), [vladimir.brailovski@etsmtl.ca](mailto:vladimir.brailovski@etsmtl.ca)

### **ABSTRACT**

Water atomized iron powders with different particle size distributions were compared to the benchmark gas atomized stainless steel powders in terms of their granulometry, particle morphology, Hausner ratio, and cohesion strength. The iron powders were evaluated for structural analysis (porosity, volume shrinkage) and mechanical testing (transverse rupture strength) by producing rectangular prismatic specimens via the binder-jetting additive manufacturing and conventional compaction technologies. This work demonstrates that the water atomized powders provide a viable alternative to their gas atomized counterparts as a binder-jetting additive manufacturing feedstock.

### **INTRODUCTION**

It has been unequivocally established that the mechanical properties of components produced by powder-bed additive manufacturing (AM) technologies, such as selective laser/electron beam melting (SLM/EBM) and binder-jetting (BJ), depend on the powder layer density. The higher this density, the higher the density of the final product, and, therefore, its mechanical properties [1].

The powder-bed density is a function of mean particle size, size distribution, shape, and the type of the spreading mechanism. Spherical particles with narrow particle size ranges are generally preferred since they exhibit low interparticle friction and high mobility, and, therefore, good flowability [2]. Preferred particle size distribution ranges from 30 to 50  $\mu\text{m}$  for the SLM and BJ technologies, and from 50 to 70  $\mu\text{m}$  for the EBM technology. These size ranges stem from a compromise: decreasing the particle size results in thinner layers, better surface finish and higher part accuracy; however, these benefits are reached at the expense of higher friction and electrostatic forces negatively affecting powder spreading and handling [3].

The excellent morphological characteristics of gas atomized metal powders make them highly suitable for powder-bed AM systems, but their high cost represents one of the major obstacles for a larger industrial use of AM technologies in general. From a cost-efficiency perspective, therefore, water atomized powders would be a viable alternative to their gas atomized counterparts, provided the former possess sufficient flowability and lead to high powder-bed density [2].

To date, the number of studies on the suitability of water atomized powders for AM is still very limited [2, 4-6]. This work focuses on the use of water atomized iron powders for the binder-jetting additive manufacturing process.

---

\*Corresponding author

## EXPERIMENTAL

Commercially available water atomized iron powders (Rio Tinto Metal Powders (RTMP), also known as QMP, Sorel-Tracy, Canada) were used as powder feedstock in an M-Flex Binder Jetting system (ExOne, USA). Prior to their use, QMP powders with a true density of  $7.87 \text{ g/cm}^3$  were additionally treated to yield two powder batches, designated as A and B. ExOne's gas atomized SS430 stainless steel powder was used as a reference feedstock.

### Powder characterization

The following powder characteristics were evaluated: particle size distribution, circularity, apparent and tap density, shear torque and cohesion strength.

- The particle size distributions ( $D_{10}$ ,  $D_{50}$ ,  $D_{90}$ ) of powders A, B and SS430 were measured using a Mastersizer 3000 laser diffraction particle size analyzer. The mean, mode and median particle circularity were calculated using “frequency-circularity” distribution diagrams obtained from the numerical analysis of SEM images using the morphology evaluation algorithm [7]. The particle circularity index (CI) was quantified as  $CI = 4\pi A/P^2$ , where P is the perimeter, and A is the surface area of each particle within the analysed particle population (CI equals 1 for a perfect circle).
- The apparent ( $\rho_a$ ) and tap ( $\rho_t$ ) powder densities were measured as follows: first, a 50 g weight powder specimen was placed in a graduated cylinder to measure its apparent volume ( $V_a$ ). Next, using a vibrating table, the powder was tapped (the tapping was considered as done when no volume changes under vibration were observed) in the same cylinder to measure the tap volume ( $V_t$ ). Finally, using the calculated apparent and tap density values, the Hausner ratio was evaluated as  $\rho_t/\rho_a = V_a/V_t$  [8-10].
- The shear torque and cohesion strength of powders were measured using a Modular Compact Rheometer (Anton Paar, USA) equipped with a “Powder Cell” accessory [8]. 100 mL of powder was loaded in the cell, fluidized at an air flow rate of 5 L/min for 60 seconds, and measured, using a two-bladed stirrer at a rotational speed of 8 rpm. The conversion from torque to cohesion strength was established by multiplying the torque by a geometry-dependent CSS factor: “Cohesion strength=Torque\*CSS”, where  $CSS=0.0124$  (measuring system parameter) [9].

### Geometry, printing and post-printing treatments of BJ-printed specimens

Rectangular prismatic  $31.7 \times 12.7 \times 6.35 \text{ mm}$  ( $1.25 \times 0.5 \times 0.25 \text{ inch}$ ) transverse rupture strength (TRS) specimens (MPIF Standard No.41) [9] were BJ-printed for porosity evaluation and 3-point bend test (Figure 1). The as-printed “green” specimens were subjected to a sequence of two thermal treatment procedures: a) curing, leading to “brown” specimens and b) sintering, to yield the final product. Several specimens were sintered in a furnace under atmospheric pressure, and in a hot isostatic press (HIP). The recoating parameters (layer thickness and speed of powder recoating device) recommended for stainless steel by ExOne were optimized to ensure homogeneous powder spread.

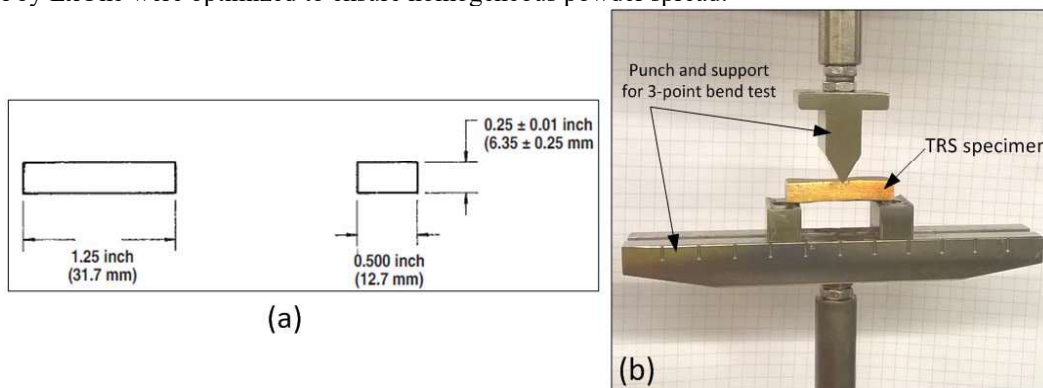


**Figure 1.** TRS specimen dimensions (a) and 3-point bend test setup (b)

Curing was done in a curing oven (JPW Design & Manufacturing) at 195°C for six hours under atmospheric conditions. Furnace sintering was performed in an H41-Nfurnace (Nabertherm, Germany) at 1100°C for two hours under argon flow (10-20 l/h). Selected “brown” specimens were subjected to bronze infiltration, using the same time/temperature conditions. Finally, HIP sintering was performed in a Quintus QIH-3 graphite furnace (AVURE, USA) at 1100, 1200 and 1300 °C for two hours and two pressure regimes: 100 and 150 MPa (14.5 and 22 ksi) in argon.

The volume and weight of the printed and post-processed specimens were measured by a calliper (Mitutoyo, Japan) (precision of 0.01 mm) and a balance (AND EK-120i, max 120g, precision of 0.01 g). Next, their bulk ( $\rho$ ) and relative ( $\rho/\rho_{\text{true}}$ ) densities and porosity ( $1 - \rho/\rho_{\text{true}}$ ) were calculated. In a similar way, the volume shrinkage occurring during sintering, hot isostatic pressing and infiltration was calculated with respect to the “brown” volume ( $V_{\text{“brown”}} - V / V_{\text{“brown”}}$ ).

According to ASTM B528-12, three-point mechanical bend test with a crosshead speed of 0.197 inch/min was performed on as-printed, cured, furnace-sintered, HIPed and infiltrated specimens (3 specimens were tested for each experimental condition) using a Minibionix 858 testing machine (MTS, USA) [10]. The TRS was calculated using the following equation:

$$TRS: \sigma = \frac{3Fl}{2bh^2} \quad (1)$$

where F is the force required to rupture the specimen; l is the distance between the centers of the supporting rods; b and h are the specimen width and thickness, respectively.

For comparison, several TRS specimens were prepared from B-type powders using the conventional compaction powder metallurgy process (PM compaction). F-0000<sup>†</sup> TRS bars were compacted with 0.3% internal lubricant (wax) and manual die-wall lubrication (ZnSt spray). “Green” density of these specimens was 7, 7.2 and 7.4 g/cm<sup>3</sup>. The green specimens were subjected to furnace sintering at 1120°C for 30 min in an 90%N<sub>2</sub>/10%H<sub>2</sub> atmosphere as well as to copper infiltration [11]. The TRS of these specimens were measured and compared to that of their BJ-printed counterparts.

The residual porosity of the bronze infiltrated BJ-printed specimens ( $P_{\text{infiltrated}}$ ) was calculated on rectangular TRS specimens. First, the weight and volume of the as-cured and infiltrated specimens were measured. It was assumed that the difference between the weights corresponds uniquely to the bronze (copper) gain during infiltration sintering. Infiltrated specimen volume was multiplied by porosity of initial (as-cured) specimen ( $P_{\text{as-cured}}$ ) to evaluate the volume of pores filled with bronze to create completely dense specimen ( $V_{\text{infiltrated, dense}}$ ). The infiltrated bronze/copper weight and its bulk density were used to calculate the infiltrated volume ( $V_{\text{infiltrated, porous}}$ ) and compared to  $V_{\text{infiltrated, dense}}$  according to the following equation:

$$P_{\text{infiltrated}} = (1 - V_{\text{infiltrated, dense}}/V_{\text{infiltrated, porous}}) \cdot P_{\text{as-cured}}$$

## RESULTS

**Particle size distributions and morphology of the powder feedstock.** The particle size and distribution are plotted in Figure 2a, b, while their circularity is shown in Figure 2c. It can be observed that particle size distributions of powders A and B are similar and these powders exhibit larger dispersion and contain more fine particles than the gas-atomized SS 430 powder. Furthermore, the morphology analysis allows a clear distinction between the powder batches (Figure 2c): the gas atomized SS 430 powder stands out from its water atomized counterparts; the majority of the SS430 powder particles are spherical (mean

<sup>†</sup> Material Designation Code for unalloyed PM iron in Materials Standards for PM Structural Parts, MPIF Standard 35 - 2012 Edition.

circularity is close to 0.80), while the shapes of the A and B powder particles are much less regular (their mean circularities are about 0.65 and 0.67, respectively). The results of the particle size distribution and morphology analyses are grouped in Table 1.

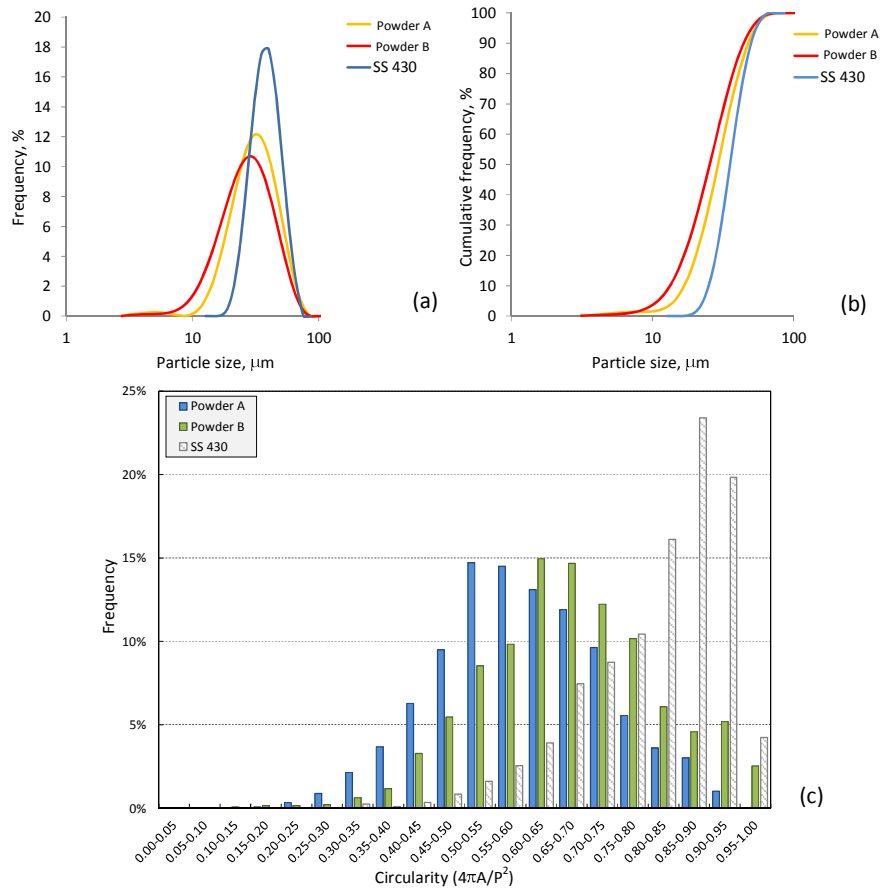


**Figure 2.** Powders A, B and SS 430: (a) particle size distribution, (b) cumulative frequency distribution (b), and (c) powder particle circularity frequency distribution

**Table 1.** Characteristics of the feedstock powders (W.A.=water-atomized, G.A.=gas-atomized)

Characteristics		W.A. Powder A	W.A. Powder B	G.A. SS 430
Granulometry, $\mu\text{m}$	D <sub>10</sub>	19	15.2	28.3
	D <sub>50</sub>	33.1	29.1	40.4
	D <sub>90</sub>	54.6	50.7	57.2
Circularity	Mean	0.65	0.67	0.81
	Mode	0.50-0.55	0.60-0.65	0.85-0.90
	Median	0.55-0.60	0.62	0.75
Density, $\text{g}/\text{cm}^3$	Apparent	3.03	3.49	4.39
	Tap	3.83	3.99	4.79
Hausner ratio (HR)*		1.27	1.14	1.09
Torque, $\text{mN}\cdot\text{m}$		100	90	65
Cohesion strength, $\text{kPa}$		1.25	1.15	0.8

\* HR<1.25 - good flowability; HR>1.45 - poor flowability [12].

**Apparent, tap density and Hausner ratio.** The ratio of the apparent and tap densities, represented by the Hausner ratio, estimates the flowability and compaction capacities of the powders: the closer the Hausner ratio is to unity, the better the flowability and the worse the compaction capacity of the powder blend. It can clearly be observed from Table 1 that the flowability potential of the water atomized powders is slightly lower than that of their gas atomized counterpart.

**Powder rheology measurements.** First, the torque needed to shear the powder layer in a rheometer cell equipped with a stirrer is measured, and this measurement makes it possible to calculate the friction forces resisting the powder flow (cohesion strength). The lower the torque and the cohesion strength, the easier it is for the powder to be evenly spread by different powder spreading systems, such as blade- or roller-based spreading mechanisms, feed hoppers, etc. The results obtained with powders A, B and SS 430 corroborate the previous conclusion on a higher relative flowability of the gas atomized SS 430 powders (Figure 3).

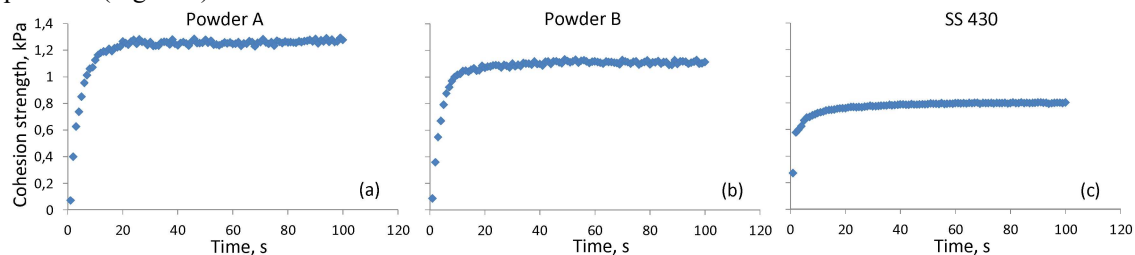


**Figure 3.** Cohesion strength (a-c) vs time for A (a), B (b) and SS 430 (c) powders

In summary, a strong correlation exists between the powder morphology and its flowability potential: the higher the particle circularity, the better the powder flowability (Table 1). On the basis of these results, to facilitate uniform spreading, increased powder bed density and, therefore, improved mechanical properties of the final product, less irregular and dispersed water atomized B-type iron powder was selected for the next step of this work, BJ printing and PM compaction.

**Volume shrinkage and TRS.** Figure 4 summarizes the porosity, volume shrinkage and mechanical strength data obtained with specimens printed from the B-type powder. The porosity of “green” TRS specimens made from the B-type powders is about 60%, which is close to the ~55% porosity obtained with the benchmark SS430 powders.

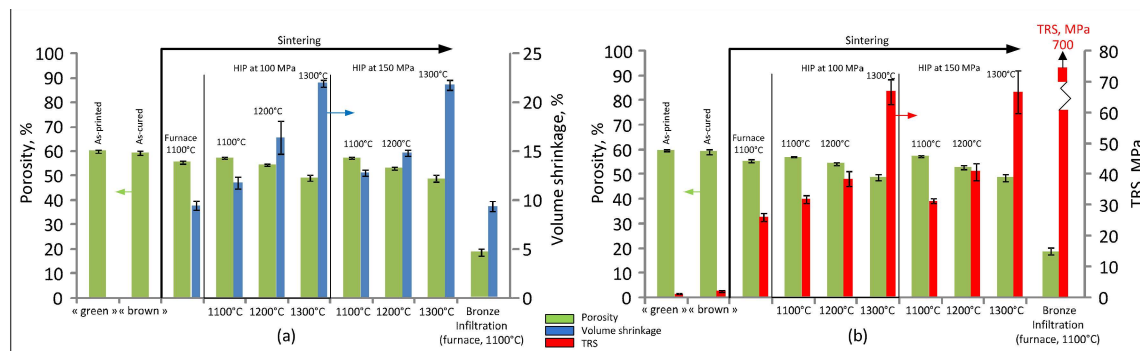


**Figure 4. Printed (BJ) TRS specimens (B powder):** porosity versus volume shrinkage (a) and porosity versus mechanical resistance (b)

As expected, the “green” and “brown” BJ-printed specimens are very weak (TRS < 5 MPa or 0.7 ksi). Furnace sintering (1100 °C) burns the binder and creates metallic bonds between particles, thus increasing TRS up to 26 MPa (3.7 ksi). The volume shrinkage effect is close to 10%, while porosity does not change notably. HIP sintering at 1100°C with an applied pressure of 100...150 MPa (14.5...22 ksi) results in a

23% higher TRS and 30% higher shrinkage, while the porosity is still close to 55%. Generally speaking, the higher the HIP temperature and pressure, the higher the expected shrinkage, the lower the porosity and the higher the mechanical resistance. In our case however, an increase in HIP temperature plays much greater role in the shrinkage, porosity and mechanical properties evolution than an increase in HIP pressure (Figure 4).

TRS of the sintered specimens produced via a “standard” QMP PM compaction route depends on their “green” (compacted) density. When the green density increases from 7 to 7.2 and 7.4 g/cm<sup>3</sup>, TRS increases from 406±2 MPa (59±0.3 ksi) to 463±14 MPa (67±1.7 ksi) and 553±10MPa (80±1.4 ksi) respectively (Figure 5). These values are 10-20 times higher than those of the sintered BJ-printed specimens because their porosity is significantly lower: 5-10% for the as-compacted specimens versus 55% for the as-printed specimens.

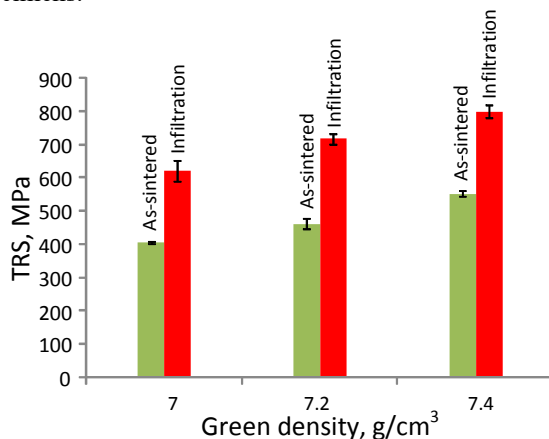


**Figure 5.** Mechanical resistance of PM compacted RTMP TRS specimens of different green density after sintering and infiltration procedures

Infiltration with copper of the compacted and with bronze of the printed specimens improves their mechanical resistance, but to a different extent: this improvement is much greater for the latter as compared to the former. Figure 5 shows that for the same green density of 7 g/cm<sup>3</sup>, TRS of the infiltration-sintered compacted specimens is approximately 1.5 times greater than that of the just-sintered compacted specimens: 621±31 MPa (90±4.5 ksi) versus 406±2 MPa (59±0.3 ksi). The higher the green density of the compacted specimens, the greater their mechanical resistance after infiltration sintering: TRS of the specimens with green density of 7.2 and 7.4 g/cm<sup>3</sup> becomes 719±16 MPa (103±2.3 ksi) and 801±18 MPa (116±2.6 ksi) after this processing. TRS of the infiltration-sintered printed specimens becomes almost 25-times higher than that of their just-furnace-sintered counterparts: 700 MPa (101 ksi) versus 26 MPa (3.7 ksi) (Figure 4b). The greater degree of improvement due to infiltration sintering shown by printed specimens is mainly due to their significantly lower green density as compared to that shown by their compacted counterparts.

## CONCLUSIONS

1. The results of the particle size, morphology, density and rheology analyses of the water and gas atomized powders are strongly correlated: the higher the circularity and the narrower the particle size distribution, the higher the powder flowability, the latter being evaluated in this work by the Hausner ratio and the cohesion strength numbers.
2. Even though the flowability of the water atomized powders is inferior to that of their gas atomized counterparts, the porosity of the specimens printed from the QMP water atomized iron powder is close to that of the ExOne gas atomized SS430 powder (~60 versus ~55%).

3. Hot isostatic pressing of the BJ-printed specimens increases their TRS from 5 to 70 MPa. Volume shrinkage effect varies according to the HIP procedure between 12 and 22%.
4. The TRS of the BJ-printed bronze-infiltrated specimens is almost 25-times higher than that of their just-furnace-sintered counterparts: 700 versus 26 MPa.
5. TRS of the printed and bronze-infiltrated specimens falls within the TRS range of their compacted and copper-infiltrated counterparts: 700 MPa compared to 600...800 MPa. In summary, this work demonstrates that the water atomized powders provide a viable alternative to gas atomized powders as a binder-jetting additive manufacturing feedstock.

### ACKNOWLEDGMENTS

This project is supported by the Natural Sciences and Engineering Research Council of Canada. The authors would like to thank Anton Paar, and, especially, James P. Eickhoff Jr. and Mélina Hamdine for their contribution in the realization of this rheological study.

### REFERENCES

1. Verlee, B., Dormal, T., Lecomte-Beckers, J. , *Density and porosity control of sintered 316L stainless steel parts produced by additive manufacturing*. Powder Metallurgy, 2012. **55**(4): p. 260-267.
2. Schade, C.T., Murphy, T.F., Walton, C. . *Development of atomized powders for additive manufacturing*. in *MPIF World Congress on Powder Metallurgy and Particulate Materials*. 2014. Orlando, FL.
3. Karapatis, N.P., Egger, G., Gyax, P.-E., Glardon, R. . *Optimization of powder layer density in selective laser sintering*. in *9th Solid Freeform Fabrication Symposium*. 1999. Austin (USA).
4. Hoeges, S., Schade, C.T., Causton, R. *Development of a maraging steel powder for additive manufacturing*. in *MPIF World Congress on Powder Metallurgy and Particulate Materials*. 2015. San Diego, CA.
5. Zhou, Y.S., S.C., Orange, M., Schade, C., Garcia, C.I. *Sintering behavior of componenets produced by additive manufacturing using gas versus water atomized 420 stainless steel powders*. in *Materials Science and Technology (MS&T)*. 2014. Pittsburgh, Pennsylvania, USA: MS&T14.
6. Pinkerton, A.J., Li, L. , *Direct additive laser manufacturing using gas- and water-atomised H13 tool steel powders*. Int J Adv Manuf Technol 2005. **25**: p. 471-479.
7. Murphy, T.F., *Metallographic testing of powders intended for use in additive manufacturing*. 2015.
8. Anton Paar, c., *SLS Powder Analysis with the Anton Paar Powder Cell*, in *D431A001EN-A*. 2015, Anton Paar.
9. Mezger, T.G., *The Rheology Handbook: For Users of Rotational and Oscillatory Rheometers*. 2006: Vincentz Network GmbH & Co KG. 299.
10. ASTM, *B528 – 12, Standard Test Method for Transverse Rupture Strength of Powder Metallurgy (PM) Specimens*. 2012, ASTM international.
11. RioTinto, *Powder specification brochure*.
12. Geldart, D., Abdullah, E.C., Hassanpour, A., Nwoke, L.C., Wouters, I., *Characterization of powder flowability using measurement of angle of repose*. China Particuology, 2006. **4**(3-4): p. 104-107.